Estimation of the Flood Area Using Multi-temporal RADARSAT SAR Imagery

Hong-Gyoo SOHN*, Yeong-Sun SONG**, Hwan-Hee YOO*** and Won-Jo JUNG****

Abstract

Accurate classification of water area is an preliminary step to accurately analyze the flooded area and damages caused by flood. This step is especially useful for monitoring the region where annually repeating flood is a problem. The accurate estimation of flooded area can ultimately be utilized as a primary source of information for the policy decision.

Although SAR (Synthetic Aperture Radar) imagery with its own energy source is sensitive to the water area, its shadow effect similar to the reflectance signature of the water area should be carefully checked before accurate classification. Especially when we want to identify small flood area with mountainous environment, the step for removing shadow effect turns out to be essential in order to accurately classify the water area from the SAR imagery.

In this paper, the flood area was classified and monitored using multi-temporal RADARSAT SAR images of Ok-Chun and Bo-Eun located in Chung-Book Province taken in 12th (during the flood) and 19th (after the flood) of August, 1998.

We applied several steps of geometric and radiometric calculations to the SAR imagery. First we reduced the speckle noise of two SAR images and then calculated the radar backscattering coefficient (σ^0). After that we performed the ortho-rectification via satellite orbit modeling developed in this study using the ephemeris information of the satellite images and ground control points. We also corrected radiometric distortion caused by the terrain relief. Finally, the water area was identified from two images and the flood area is calculated accordingly. The identified flood area is analyzed by overlapping with the existing land use map.

Keywords : RADARSAT SAR, Flood Area, Radar Backscattering Coefficient, Shadow Effect

1. Introduction

SAR is capable of acquiring high-resolution images in all weather and all-day conditions with its active microwave systems. Moreover, the returned waves sensitive to the ground features make it possible to get additional information not available in optic sensors. For this reason, we could get better quality of image information by combining data obtained from SAR and optic sensors[1].

SAR data have been opened to the public since the union of 13 European countries launched ERS-1 in 1991 while the researches on them have begun since 1960's. Including JERS-1 of Japan in 1992 and RADARSAT of Canada in 1995, there were a series of satellites carrying SAR, which accelerated researches on observation and application with them. A variety of researches have been performed using SAR images such as agriculture, forestry, water resources, ocean research, and disaster prevention[2].

Especially in the application of flood disaster, SAR is very useful due to its capability of acquiring images in bad weather condition while optic sensors can not. Analysis of flood range and distribution of the Yangtze, the north of China[3], in 1998, flood damage mapping in North Korea[4], and determination of inundation areas as well as low drainage areas of the Lesse in Belgium are good examples using SAR[5] for flood estimation. Though multi-temporal RADARSAT SAR images have been used for observing the peninsula

by a series of wood fire in KangWon on April 2000, Korea[6], that many applications have not made comparing to those of optic sensors.

In this research, we try to estimate the flood area monitored by RADARSAT SAR imagery obtained at the time of the flood and after the flood. For this, together with satellite images, land use maps have been utilized for accurate estimation of flood area. We believe that this research can be ultimately applied to the quick estimation of flood damage and policy decision for flood related disasters repeating every year.

2. Study Area and Data Sets

YANNI and PENNY, two of the 16 typhoons formed in 1998, caused a great deal of damages to Korean peninsula. Especially typhoon PENNY poured plenty of rain in the areas of Mt. SokLee and Bo-Eun, so that

cities and farms of Ok-Chun and Bo-Eun were seriously damaged by the inundation[7]. Daily precipitation record in those areas is shown in Figures 3 and 4 (Korean Meteorological Administration), and regional trends of the rainfall in August are shown in Figure 1.

As shown in Figures 3 and 4, a localized torrential downpour has begun on August 12 and ended on August 19, 1998. Since our research objective is to find out the signature of this heavy rainfall from SAR imagery, we acquired two SAR images, one of which is acquired on August 12 in the middle of the downpour, and the other of which is acquired on August 19 after the downpour.

We used 100km × 100km SAR images of SGF (SAR Georeferenced Fine resolution, 16 bit) with standard beam 6 (1998/08/12) and beam 5 (8/19/1998) whose resolution are 25m×25m and are in ascending mode (Figures 5 and 6).
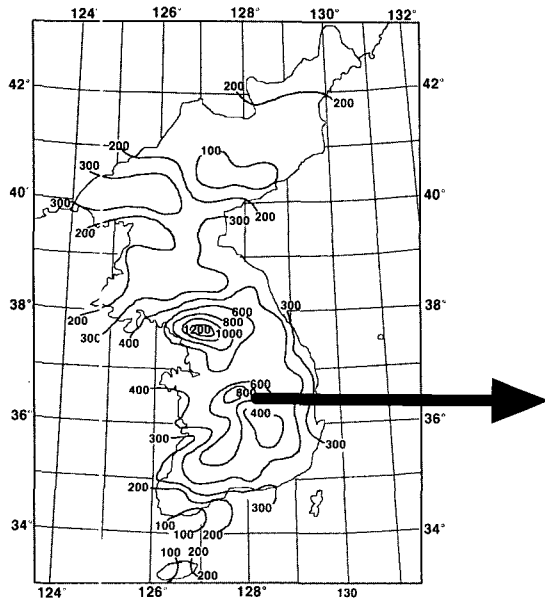

Fig. 1. Regional rainfall distribution in August.

Fig. 2. Cities and farms inundated by the flood from July 30 to August 12 in Bo-Eun Chung-Book province.
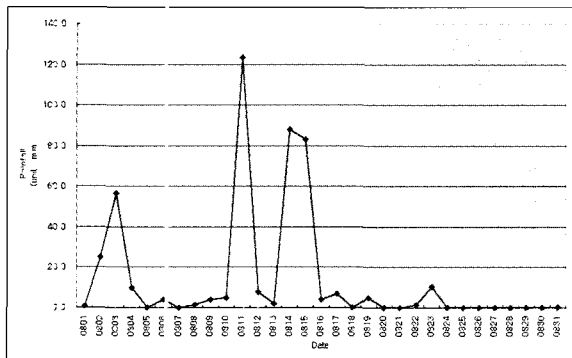

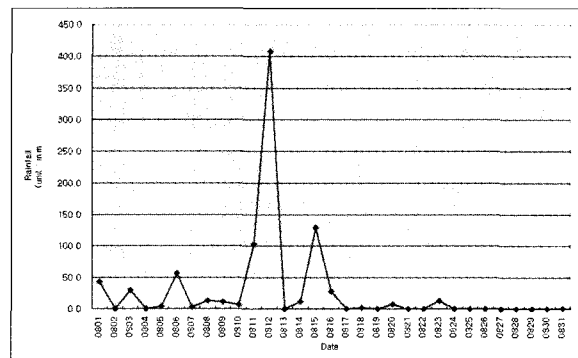Fig. 3. Precipitation record of Ok-Chun.

Fig. 4. Precipitation record of Bo-Eun.

Fig. 5. August 12, 1998 SAR image (SGF, S6, 8724×
8630, 16bit, during the flood).

Fig. 6. August 18, 1998 SAR image (SGF, S5, 8979×
8441, 16bit, after the flood).

3. Calculation of Geometric and Radiometric Parameters

3.1 Calculation of Radar Backscattering Coefficient

Reduction of the speckle noise from a SAR image is one of the essential processes to improve the quality of the classification accuracy. We applied Lee-sigma filter with window size of 5×5 for this purpose. To perform the classification after reducing the speckle noise, σ^0 (a radar backscatter coefficient) is used instead of original 16 bit DN (digital number) value. β^0 (radar brightness) is calculated to determine σ^0 using the following equation[8]

$$\beta_j^0 = 10 \times \log_{10}[\,(DN_j^2 + A_3)/A_{2j}] \tag{3-1}$$

where, A_{2j} is the scaling gain value of the jth pixel in slant range direction determined by interpolating 512 LUT values given at the header, and A_3 is the scaling offset, and DN_j is the digital value of the jth pixel. The relationship between radar brightness(β_j^0) and radar backscattering coefficient is given by

$$\sigma_j^0 = \beta_j^0 + 10 \log_{10}(\sin I_j) \tag{3-2}$$

where, I_j is the incidence angle at the jth range pixel. This formula assumes that the earth is smooth ellipsoid at sea level. Calculation of I_j is done by using the formula given by
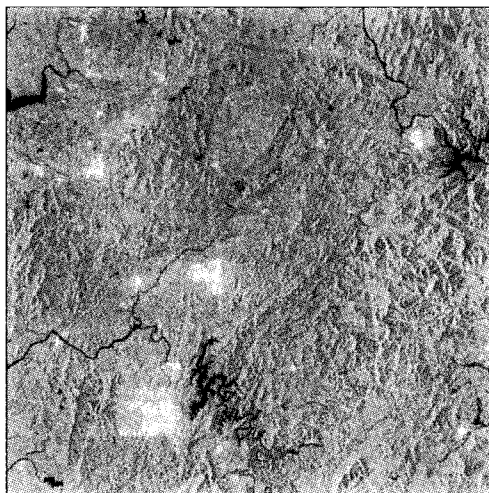

Fig. 7. Radar backscattering coefficient image (8/12/
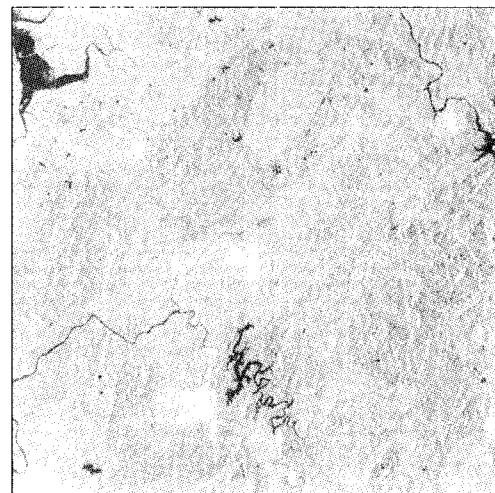1998, size 8724×8630, 16bit).

Fig. 8. Radar backscattering coefficient image (8/19/
1998, size 8979×8441, 16bit).

$$I_j = \cos^{-1}[-\frac{(h^2-(r_j)^2+2 \cdot R \cdot h)}{2 \cdot r_j \cdot R}] \qquad (3-3)$$

where, R is the earth radius at image center position, and h is the orbit altitude, and r_j is the slant range of the jth pixel. The transformation from the ground range to the slant range is performed as follows;

$$r_j = a + j \cdot dRg \cdot b + (j \cdot dRg)^2 \cdot c + (j \cdot dRg)^3 \cdot d$$
$$+ (j \cdot dRg)^4 \cdot e + (j \cdot dRg)^5 \cdot f \qquad (3-4)$$

where, a, b, c, a, e, f are transformation coefficient from the ground range to the slant range and dRg is the ground range resolution of the image.

The calculated radar backscattering coefficient ranges -40.49~8.32dB in the August 12th image and -42.98~9.60dB in the August 19th image, respectively (see Figure 7 and 8). Most of the dark areas in Figures 7 and 8 correspond to the water area of low dB.

3.2 Ortho-rectification of RADARSAT SAR Images

3.2.1 Calculation of Orbit Models

Exact estimation of satellite position is one of the crucial procedures for the ortho-rectification and the radiometric slope correction. The geometry of SAR images is expressed as both the slant range equation between a target and a satellite (Equation 3-5) and the Doppler centroid equation (Equation 3-6)[9].

$$r = |\vec{p} - \vec{s}| \qquad (3-5)$$

$$f_{DC} = \frac{2(\vec{p} - \vec{s}) \cdot (\vec{p'} - \vec{s'})}{\lambda |\vec{p} - \vec{s}|} \qquad (3-6)$$

In above equations, a target position vector($\vec{p}$) is $(P_x, P_y, P_z)^T$ expressed in the geocentric coordinate system. The target velocity vector($\vec{p'}$) can be calculated $\vec{\omega}_e \times \vec{p}$ in inertial coordinate system and $\vec{\omega}_e(-P_y, P_x, 0)^T$ in geocentric coordinate system. $\vec{\omega}_e$ is an earth rotation rate of $2\pi/(24 \times 3600)$ sec, and λ is a wave length[10],[11]. $\vec{s}$, the position vector of the satellite, can be expressed as in Equation 3-7 considering the second order term of time t.

$$S_x(t) = a_1 + a_2 t + a_3 t^2$$
$$S_y(t) = b_1 + b_2 t + b_3 t^2$$
$$S_z(t) = c_1 + c_2 t + c_3 t^2 \qquad (3-7)$$

If we differentiate Equation 3-7 with respect to the time t, we can express a velocity vector of the satellite

$\vec{s'}$ as follows

$$S'_x = a_2 + a_3 t$$
$$S'_y = b_2 + b_3 t$$
$$S'_z = c_2 + c_3 t \qquad (3-8)$$

Slant range r is determined by either using the coefficient (Equation 3-4) or using both coefficient between the slant range and the ground range given by its header and range sampling rate as

$$r_j = a + j \times \frac{c(speed\ of\ light)}{2.0 \times Range\ Samping\ Rate} \qquad (3-9)$$

where, a is the same as that of Equation 3-4. The Doppler centroid frequency is calculated with the data given by the header and Equation 3-10, where d_0, d_1, d_2 are cross track Doppler frequency terms.

$$f_{DC} = d_0 + d_1 j + d_2 j^2 \qquad (3-10)$$

Equations 3-5 and 3-6 can be written in the form of Equations 3-11 and 3-12, which can be linearized to calculate parameters using the Taylor series (see Equation 3-13 and Equation 3-14) and can be used for the least square adjustment with ground control points (see Equation 3-15).

$$F_1(S_x, S_y, S_z) = r - |\vec{p} - \vec{s}| = 0 \qquad (3-11)$$

$$F_2(S_x, S_y, S_z) = f_{DC} - \frac{2(\vec{p} - \vec{s}) \cdot (\vec{p'} - \vec{s'})}{\lambda |\vec{p} - \vec{s}|} = 0 \qquad (3-12)$$

$$F_1(S_{x0}, S_{y0}, S_{z0}) + \frac{\partial F_1}{\partial a_{10}} \Delta a_1 + \frac{\partial F_1}{\partial a_{20}} \Delta a_2 + \frac{\partial F_1}{\partial a_{30}} \Delta a_3$$
$$+ \frac{\partial F_1}{\partial b_{10}} \Delta b_1 + \frac{\partial F_1}{\partial b_{20}} \Delta b_2 + \frac{\partial F_1}{\partial b_{30}} \Delta b_3 + \frac{\partial F_1}{\partial c_{10}} \Delta c_1$$
$$+ \frac{\partial F_1}{\partial c_{20}} \Delta c_2 + \frac{\partial F_1}{\partial c_{30}} \Delta c_3 = 0 \qquad (3-13)$$

$$F_2(S_{x0}, S_{y0}, S_{z0}) + \frac{\partial F_2}{\partial a_{10}} \Delta a_1 + \frac{\partial F_2}{\partial a_{20}} \Delta a_2 + \frac{\partial F_2}{\partial a_{30}} \Delta a_3$$
$$+ \frac{\partial F_2}{\partial b_{10}} \Delta b_1 + \frac{\partial F_2}{\partial b_{20}} \Delta b_2 + \frac{\partial F_2}{\partial b_{30}} \Delta b_3 + \frac{\partial F_2}{\partial c_{10}} \Delta c_1$$
$$+ \frac{\partial F_2}{\partial c_{20}} \Delta c_2 + \frac{\partial F_2}{\partial c_{30}} \Delta c_3 = 0 \qquad (3-14)$$

$$Av + B_s \Delta_s + E = 0 \qquad (3-15)$$

In Equation 3-15, A is an unit vector and v is a residual vector generated by excluding the second and higher order terms in the Taylor series. B_s is a partial differential design matrix, and Δ_s is a correction vector, and E is a discrepancy vector of satellite position

Table 1. Parameters and the accuracy of the satellite position

parameters		8/12/1998 image(unit:m)			8/19/1998 image(unit:m)		
		value	std	variance of unit weight	value	std	vairance of unit weight
Sx	a_1	-2554252.461289	12.829087		-2593099.585561	10.481405	
	a_2	-10465.609773	3.554545		-8654.718799	3.031051	
	a_3	21.184020	0.270882		2.348497	0.223877	
Sy	b_1	4953490.126076	19.293647		4916060.755922	16.358893	
	b_2	7756.711706	6.754286	0.3293	6037.886103	5.765782	0.2805
	b_3	-36.430480	0.509188		-1.293642	0.417803	
Sz	c_1	3960548.894969	10.873317		3939066.269875	80.46415	
	c_2	-14538.552192	5.803832		-12036.015793	4.96174	
	c_3	-37.823517	0.487822		-7.338097	0.41471	
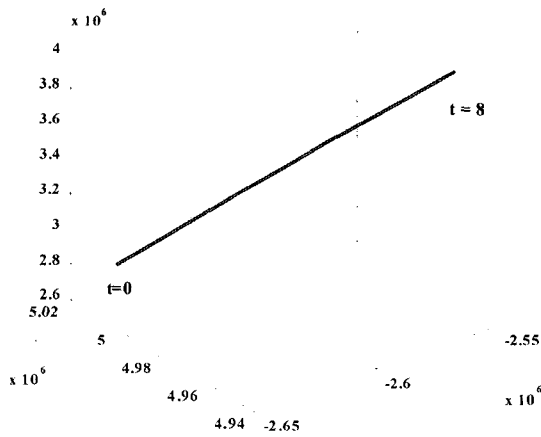
(a) 8/12/1998
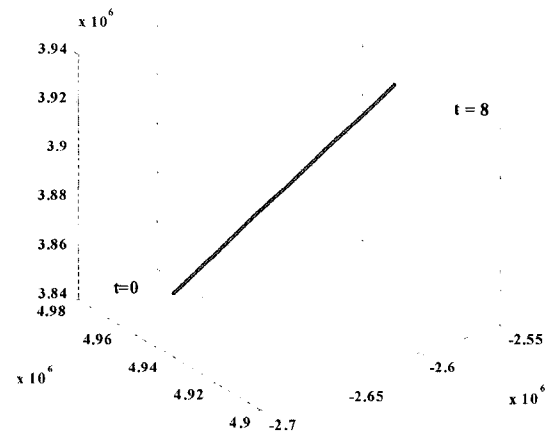
(b) 8/19/1998

Fig. 9. Orbit models of RADARSAT SAR image in geocentric coordinate system.

parameters. Assuming that the residual vector is 0, we have

$$B_s \Delta_s = -E \qquad (3\text{-}16)$$

$$\Delta_s = (B_s^T B_s)^{-1}(-B_s^T E) \qquad (3\text{-}17)$$

The adjustment procedure is iterated until the approximation of Δ_s is 0, so that the exact satellite coordinates can be calculated.

For the re-estimation of satellite orbit given in the ephemeris data we need both ground control points and initial values of satellite position. For this, ground control points are obtained from 1:5,000 digital map. Two initial values of the least square adjustment are the platform geodetic latitude for scene centre and the platform geodetic longitude for scene centre given by the image header, for which we transformed the geo-

detic coordinate system on the international ellipsoid to the geocentric coordinate system on the Bessel ellipsoid. Table 1 summarizes the parameters and their accuracies determined by the least square adjustment using 14 and 12 control points, respectively.

3.2.2 Ortho-rectification of RADARSAT SAR Images

We performed the ortho-rectification in the TM (Transverse Mercator) coordinate system using the calculated orbit modeling data. Digital elevation model used is in the resolution of 20 m. Radar backscattering coefficient are final data for the ortho-rectified image. Assuming that the line number of a RADARSAT SAR image is i and the column number is j, then i and j can be written as a function of time and the slant range

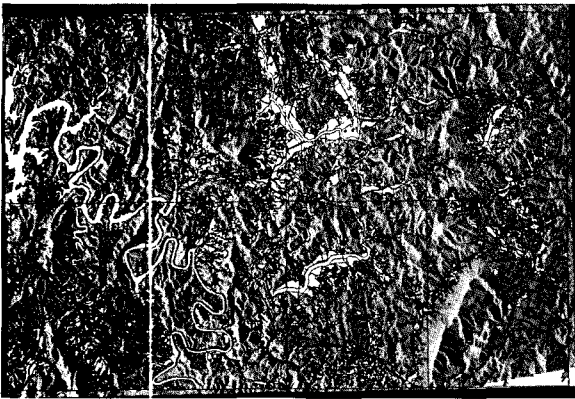$$i = \frac{t - t_{R0}}{1/PRF} \qquad (3\text{-}18)$$
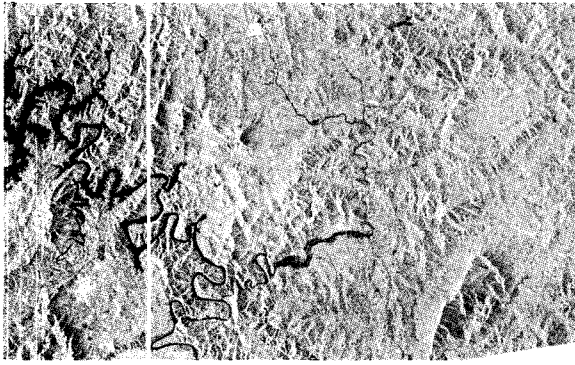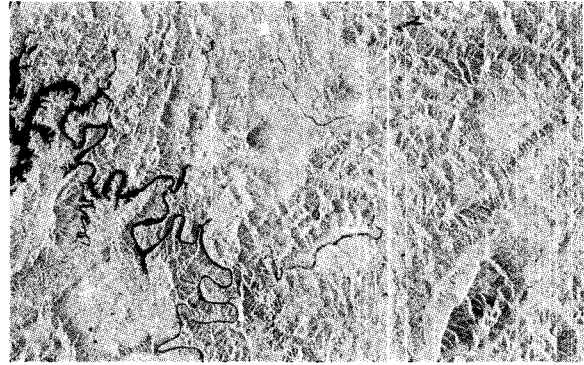
(a) 8/12/1998 (Res. 20m, size 2261×1416, 16bit)   (b) 8/19/1998 (Res 20m, size 2261×1416, 16bit)

Fig. 10. Ortho-rectified images.

(a) 8/12/1998 (Res. 20m, size 2261×1416)   (b) 8/19/1998 (Res. 20m, size 2261×1416)

Fig. 11. Overlay of ortho-rectified images with the land use map.

$$j = \frac{r - r_0}{m_r} \qquad (3\text{-}19)$$

where, t_{R0} : first slant range time

PRF : pulse repetition frequency

r_0 : slant range to near range pixel

m_r : slant range resolution.

Once the satellite position is determined, the slant range equation and the Doppler centroid shift can be written as a function of time t and the slant range r, and both of which can be linearized as a Taylor series as follows;

$$F_1(t_0, r_0) + \frac{\partial F_1}{\partial t_0} \Delta t + \frac{\partial F_1}{\partial r_0} \Delta t = 0 \qquad (3\text{-}20)$$

$$F_2(t_0, r_0) + \frac{\partial F_2}{\partial t_0} \Delta t + \frac{\partial F_2}{\partial r_0} \Delta t = 0 \qquad (3\text{-}21)$$

Further, t and r, the coordinates of RADARSAT SAR image, are expressed as

$$t = t_0 + \Delta t_0 \qquad (3\text{-}22)$$

$$r = r_0 + \Delta r_0 \qquad (3\text{-}23)$$

We iterated the above process using the initial value t_0 and r_0 until Δt and Δr become approximately 0, so that we can determine the image coordinates of DEM grids in RADARSAT SAR images. For our case, the iteration converges less than 4 times and the resulting ortho-rectification images are shown in Figure 10.

To verify the accuracy of ortho-rectified images, we overlaid them with the 1:25,000 land use map. Visual inspection of the overlaid image confirms that the water area and the mountainous area are well matched (see Figure 11).

4. Classification of Water Area and Flood Area

4.1 Radiometric Slope Correction

Both the water area and the flood area have lower

radar backscattering coefficient than those of other areas. Lower radar backscattering value, however, may be similar to that of the non-water area due to the geometric relationship between the antenna and the backscattering elements[12]. Radar backscattering coefficient as stated in Chapter 3.1 are estimated from the smooth ellipsoid at sea level. It is essential to correct the radiometric distortion caused by the terrain relief in order to improve the classification accuracy of the water area.

The radiometric distortion caused by the terrain relief is calculated with the Faceted (Lambert shading) model, which uses digital elevation models and satellite position data as input data. Local incidence angle is defined as the angle between the normal of backscattering element $\overrightarrow{n}$ and incident radiation $\overrightarrow{s}$. The local incidence angle on digital elevation models is computed using the following formula;

$$\cos(i) = \frac{-S_x a_z b_y - S_y a_x b_z + S_z a_x b_y}{\sqrt{(a_z b_y)^2 + (a_x b_z)^2 + (a_x b_y)^2}} \quad (3\text{-}24)$$

where, S_x, S_y, S_z: vector components of the incoming

radiation

a_x, b_y : grid size (constant)

a_y, b_x : 0

$$a_z = \frac{[(H_2 - H_1) + (H_3 - H_4)]}{2}$$

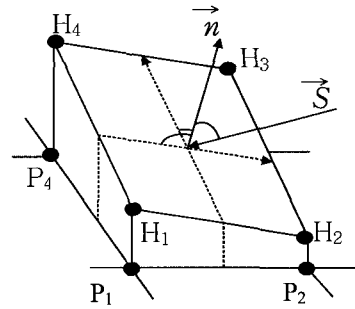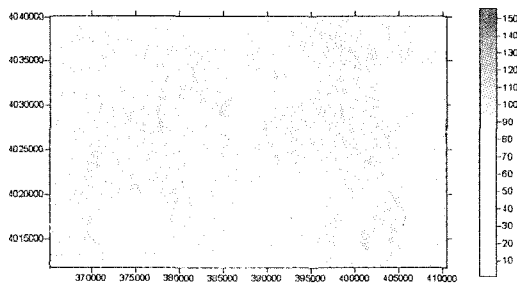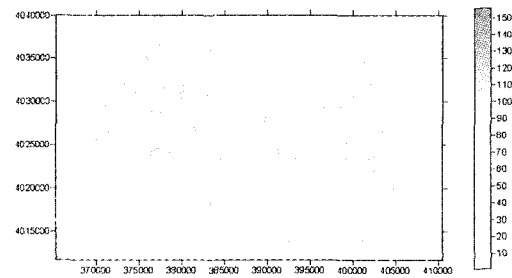$$b_z = \frac{[(H_4 - H_1) + (H_3 - H_2)]}{2}$$

Fig. 12. Geometric definition of local incidence angle.

The local incidence angle of the study area, determined by using digital elevation models and satellite orbit model, ranges from 0 to 150 degrees as shown
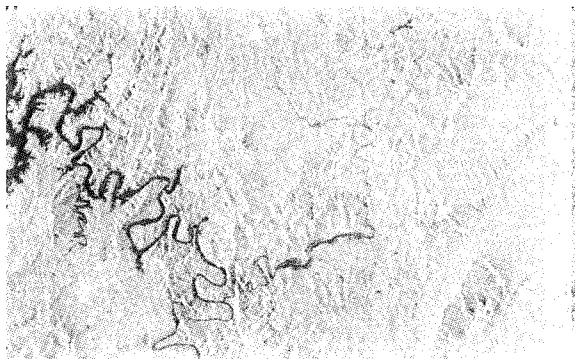
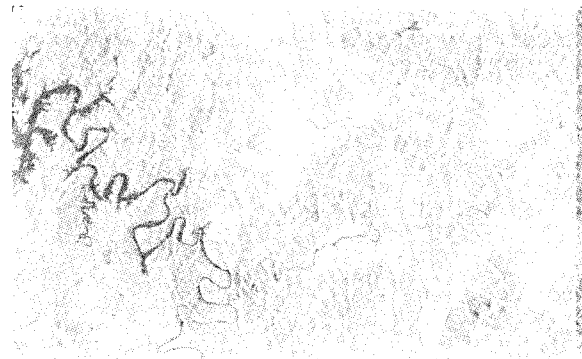(a) 8/12/1998, unit: degree (Res. 20m, size 2261×1416)   (b) 8/19/1998, unit: degree (Res. 20m, size 2261×1416)

Fig. 13. Local incidence angle map.

(a) 8/12/1998 (Res 20m, size 2261×1416, 16bit)   (b) 8/19/1998 (Res 20m, size 2261×1416, 16bit)

Fig. 14. Resulting images after the radiometric slope correction.

in Figure 13. As shown in Figure 13, the darker tones occur in the areas close to shadow area, whereas the brighter tones correspond to areas close to layover area.

The effect of radiometric distortion is corrected by dividing radar backscattering coefficient with $(\vec{S} \cdot \vec{n})^{14)}$. Figure 14 shows the resulting images after the terrain relief correction.

4.2 Water Area Classification and Flood Area Detection

Image classification is performed using the maximum likelihood method with 10 training sites. The images used for the classification are before and after the radiometric slope corrected images. As shown in Figure 15, some non-water area is classified to the water area due to the shadow area with wide incidence angle.
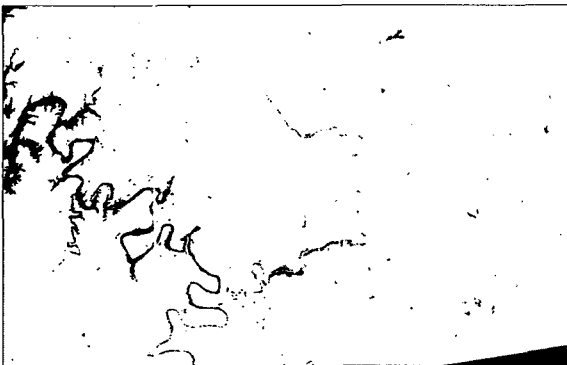

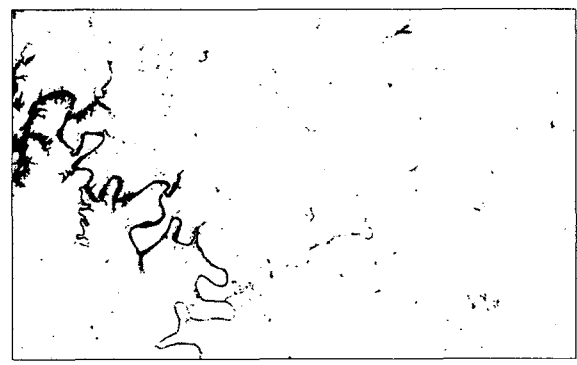(a) 8/12/1998 (Res. 20m, size 2261×1416, binary)
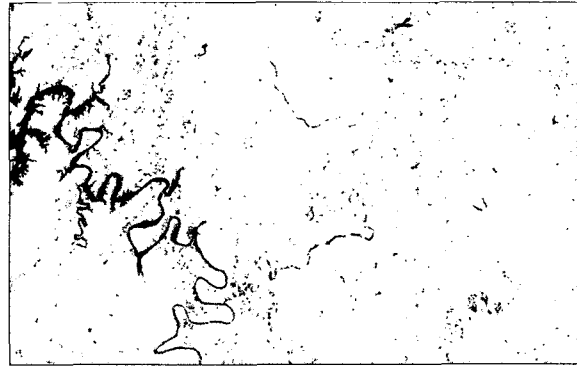
(a) 8/19/1998 (Res. 20m, size 2261×1416, binary)

Fig. 15. Water area image before the radiometric slope correction.

a. 8/12/1998 (Res. 20m, size 2261×1416, binary)

a. 8/19/1998 (Res. 20m, size 2261×1416, binary)

Fig. 16. Water area images after the radiometric slope correction.
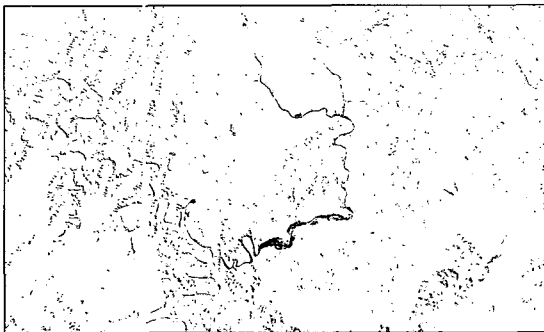

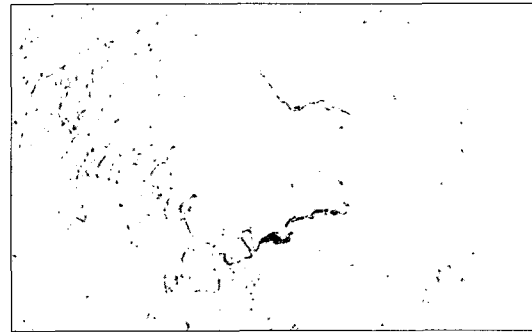Fig. 17. Flood area before the radiometric slope correction.

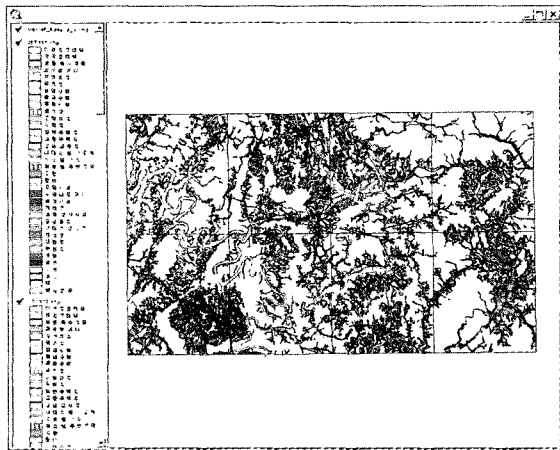Fig. 18. Flood area after the radiometric slope correction.

Fig .19. Overlay of the flood area with the digital map.

Fig. 20. Enlarged image of the flood area.

Figure 16 is the classified images after correcting the radiometric distortion. As shown in Figure 16, the classification error is considerably reduced compared to the result of Figure 15.

We extracted only the pixels classified to the water area in the August 12th image while not in the August 19th image in order to detect the flood area.

Figure 17 shows the 102770 pixels (about 4110 ha) have been detected as an increased water area before the radiometric slope correction. Figure 18 shows the 30799 pixels (about 1300 ha) have been identified an increased water area after the slope correction.

To analyze the geographical position and the land use condition of the estimated flood area, we overlaid the flood area (Figure 18) with the land use map of 1:25,000. The result is shown in Figure 19. The flood area within the range of 500m from the river is about 900ha, which is similar result of 800ha reported in the Annual Report of Disaster. In addition, we further confirmed the result by identifying that the flood area is extended to around the Dae-Chung Dam and the farm lands along the Bo-Chung river, the upper stream of the Dae-Chung Dam, as shown in Figure 20.

5. Conclusions

After classifying the water area and monitoring the flood area of Ok-Chun and Bo-Eun using the multi-temporal RADARSAT SAR images, we can reach the follwoing conclusions:

1. We successfully identified the flood area from the water area of the RADARSAT SAR images by over-lapping them with the land use map. We also observed the fact that the water area increased about 12%(1300 ha) in the study area during the flood.

2. We observed that it is possible to classify the water area more accurately only when the radiometric slope correction is performed for radar backscattering coefficient, especially of the image with the geographic features having many mountains and the small flood area like those of Korea.

3. We applied the new method to determine the orbit model required for the accurate ortho-rectification, radiometric slope correction with control points and least square adjustment.

Acknowledgements

References

1. 정 수, 1997, Radarsat위성의 위치결정과 SAR 자료의 정확도 향상에 관한 연구, 연세대학교 박사학위 논문.
2. 국방과학연구소, 1996위성영상을 이용한 3차원 정사투영 생성법에 관한 연구.
3. Shao, Y., H. Guo, H. Liu, X. Fan, J. Liao, C. Wang, S. Wang, and C. Wei, 2000, Chinese SAR for Yangtze River Flood Monitoring in 1998, IGARSS.
4. Kim, C., 2002, Flood damage Mapping in North Korea Using JERS-1 DATA, IGARSS.
5. Ormsby, J., B. Blanchard, and A. Blanchard, 1985, "Detection of Lowland Flooding Using Active Microwave Systems", PE&RS, Vol. 51, pp. 317-328.
6. Park S. E, T. H. Lee, S. Y. Hong, and W. M. Moon, 2001, Investigation of the April 2000 forest fire in Kang-won Province, Korea, using RADARSAT data, IGARSS.
7. 행정자치부 중앙재해대책본부, 1998, 재해연보.
8. RSI, 2000, .RADARSAT Data Products Specifications.
9. Schreier, G., 1993, SAR Geocoding: Data and Systems.

10. Logan. T, 1999, Calculation of ASF CEOS Metadata Values.

11. Kropatsch, W. G. and D. Strobl, 1990, The Generation of SAR Layover and Shadow Maps From Digital Elevation Models, IEEE Transaction on Geoscience and Remote sensing, Vol. 28, No. 1, pp. 98-107.

12. Small, D., F. Holecz, D. Nuesch, and A. Barmettler, 1997, Geometric and Radiometric Calibration of RADARSAT Image, Proc. of Geomatics in the Era of RADARSAT.

13. Jakob, J., van Zyl, B. D. Chapman, P. Dubies, and J. Shi, 1993, The effect of Topography on SAR Calibration, IEEE Transaction on Geoscience and Remote sensing, Vol. 31, No. 5, pp. 1036-1043.